



Data Descriptor

Comprehensive Data via Spectroscopy and Molecular Dynamics of Chemically Treated Graphene Nanoplatelets

Olasunbo Z. Farinre ¹, Hawazin Alghamdi ¹, Swapnil M. Mhatre ^{2,3}, Mathew L. Kelley ^{2,4}, Adam J. Biacchi ², Albert V. Davydov ⁵, Christina A. Hacker ², Albert F. Rigosi ², and Prabhakar Misra ^{1,*}

- Department of Physics and Astronomy, Howard University, Washington, DC 20059, USA; olasunbo.farinre@bison.howard.edu (O.Z.F.); hawazin.alghamdi@bison.howard.edu (H.A.)
- Physical Measurement Laboratory, National Institute of Standards and Technology, Gaithersburg, MD 20899, USA; swapnil.mhatre@nist.gov (S.M.M.); mathew.kelley@nist.gov (M.L.K.); adam.biacchi@nist.gov (A.J.B.); christina.hacker@nist.gov (C.A.H.); albert.f.rigosi@nist.gov (A.F.R.)
- ³ Graduate Institute of Applied Physics, National Taiwan University, Taipei 10617, Taiwan
- Theiss Research, La Jolla, San Diego, CA 92037, USA
- Material Measurement Laboratory, National Institute of Standards and Technology, Gaithersburg, MD 20899, USA; albert.davydov@nist.gov
- * Correspondence: pmisra@howard.edu

Abstract: Graphene nanoplatelets (GnPs) are promising candidates for gas sensing applications because they have a high surface area to volume ratio, high conductivity, and a high temperature stability. The information provided in this data article will cover the surface and structural properties of pure and chemically treated GnPs, specifically with carboxyl, ammonia, nitrogen, oxygen, fluorocarbon, and argon. Molecular dynamics and adsorption calculations are provided alongside characterization data, which was performed with Raman spectroscopy, X-ray photoelectron spectroscopy (XPS), and X-ray diffraction (XRD) to determine the functional groups present and effects of those groups on the structural and vibrational properties. Certain features in the observed Raman spectra are attributed to the variations in concentration of the chemically treated GnPs. XRD data show smaller crystallite sizes for chemically treated GnPs that agree with images acquired with scanning electron microscopy. A molecular dynamics simulation is also employed to gain a better understanding of the Raman and adsorption properties of pure GnPs.

Keywords: graphene nanoplatelets; spectroscopy; molecular modeling; chemical treatment



Citation: Farinre, O.Z.; Alghamdi, H.; Mhatre, S.M.; Kelley, M.L.; Biacchi, A.J.; Davydov, A.V.; Hacker, C.A.; Rigosi, A.F.; Misra, P. Comprehensive Data via Spectroscopy and Molecular Dynamics of Chemically Treated Graphene Nanoplatelets. *Data* 2022, 7, 38. https://doi.org/10.3390/data7040038

Received: 8 March 2022 Accepted: 25 March 2022 Published: 29 March 2022

Publisher's Note: MDPI stays neutral with regard to jurisdictional claims in published maps and institutional affiliations.



Copyright: © 2022 by the authors. Licensee MDPI, Basel, Switzerland. This article is an open access article distributed under the terms and conditions of the Creative Commons Attribution (CC BY) license (https://creativecommons.org/licenses/by/4.0/).

1. Introduction

The growing global concern for environmental pollution due to its negative impact on the Earth's climate and human health has led to an increased need for gas sensors with useful properties such as a high sensitivity and selectivity. These properties are crucial for identifying and removing harmful airborne contaminants from the environment. Graphene and its derivatives, such as graphene oxide, reduced graphene oxide, and carbon nanotubes, have been extensively researched for gas sensing applications due to their high surface area [1–4]. The selective chemical treatment of graphene makes them attractive for a variety of high-impact applications such as aerospace polymer reinforcement [5,6], electrical metrology [7–9], and gas sensing applications. For the latter, metal oxide semiconductors have been demonstrated to be advantageous due to their low cost, high sensitivity, and ease-of-fabrication; however, some of their drawbacks are poor selectivity, a short life span, and a high operability temperature [10].

Graphene nanoplatelets (GnPs) have become an alternative to graphene because of their potential for large-scale production while retaining properties such as excellent thermal and electrical conductivities, a high mechanical rigidity, a high aspect ratio, and light weight. GnP sheets often aggregate into flakes consisting of weakly interacting

Data 2022, 7, 38 2 of 16

monolayer sheets due to strong van der Waals attractions and strong hydrophobicity, and their functionalization leads to enhanced adsorption of target molecules (see Figure 1). GnPs have the same honeycomb structure as graphene, wherein the carbon atoms are arranged in a hexagonal ring with an atomic distance of 1.42 Å. # Each carbon atom is connected to three other neighboring carbon atoms via three σ -bonds and one π -bond (# Though not an SI Unit: This unit is permitted for expressing data by the International Committee for Weights and Measures (CIPM) and the National Institute of Standards and Technology). Recently, research studies have reported the addition of GnPs to other materials (e.g., metal oxides and polymers) to form nanocomposites in order to enhance their gas sensing abilities [11–13].

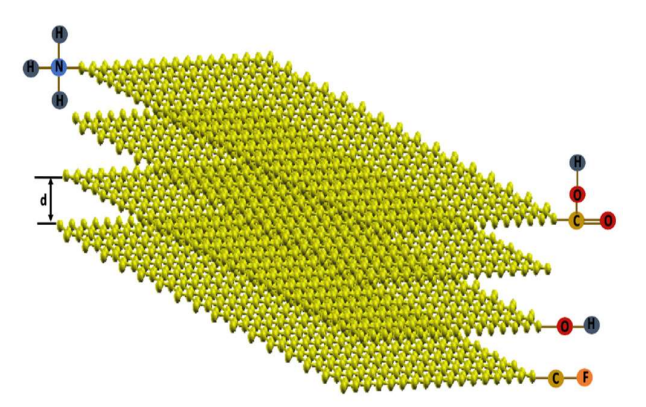


Figure 1. Diagram showing functional groups (ammonia, fluorocarbon, hydroxyl, and carboxyl) attached to the edges of one graphene nanoplatelet sheet consisting of approximately four layers of graphene. The approximate interlayer distance (d) is 3.35 Å.

In this report, a broad assessment of commercially acquired pure (untreated) and chemically treated GnPs was completed using a combination of numerical and experimental methods. For the numerical methods, molecular dynamics and adsorption simulations were performed. Experimental methods include electrical characterization, scanning electron microscopy (SEM), Raman spectroscopy, X-ray photoelectron spectroscopy (XPS), and X-ray diffraction (XRD) to identify the extent of functional group presence in each type of sample along with how such a presence affects the GnPs' surface properties. Example data acquired with Raman spectroscopy suggest the introduction of *n*-type doping when GnPs are chemically treated (35% by carboxyl functional group weight, defined as 35 g COOH per 100 g graphitic material). The effects of the full variety of functional groups on structural properties are also discussed. Untreated GnP-based devices were simulated with COMSOL o version 5.6 software to provide numerical support for expected behaviors (o Instruments, and materials are identified in this paper in order to specify the experimental procedure adequately. Such identification is not intended to imply recommendation or endorsement by the National Institute of Standards and Technology or the United States government, nor is it intended to imply that the materials or equipment identified are necessarily the best available for the purpose).

2. Data Description

2.1. Molecular Dynamics Simulations

Investigating the phonon properties requires calculating the dynamical matrix directly from molecular dynamics (MD) simulations. The dynamical matrix in Equation (1) was constructed by evaluating the displacements of atoms during the MD simulation using fluctuation–dissipation theory while taking into account the anharmonicity of phonons [14].

P-GnPs have six atoms in their primitive unit cell, therefore resulting in a total number of 18 phonon branches. As shown in Figure 2a, each type of optical phonon branch (longitudinal (LO), transverse (TO), and out-of-plane (ZO)) is split thrice, as is each acoustic

Data 2022, 7, 38 3 of 16

phonon branch (longitudinal (LA), transverse (TA), and out-of-plane (ZA)). The terms "longitudinal" and "transverse" imply that the carbon atoms are displaced in directions parallel and perpendicular to the wavevector (q) of the phonons and in plane of the platelet, respectively. The term "out-of-plane (Z)" implies the carbon atoms are displaced in directions perpendicular to the plane of the platelet.

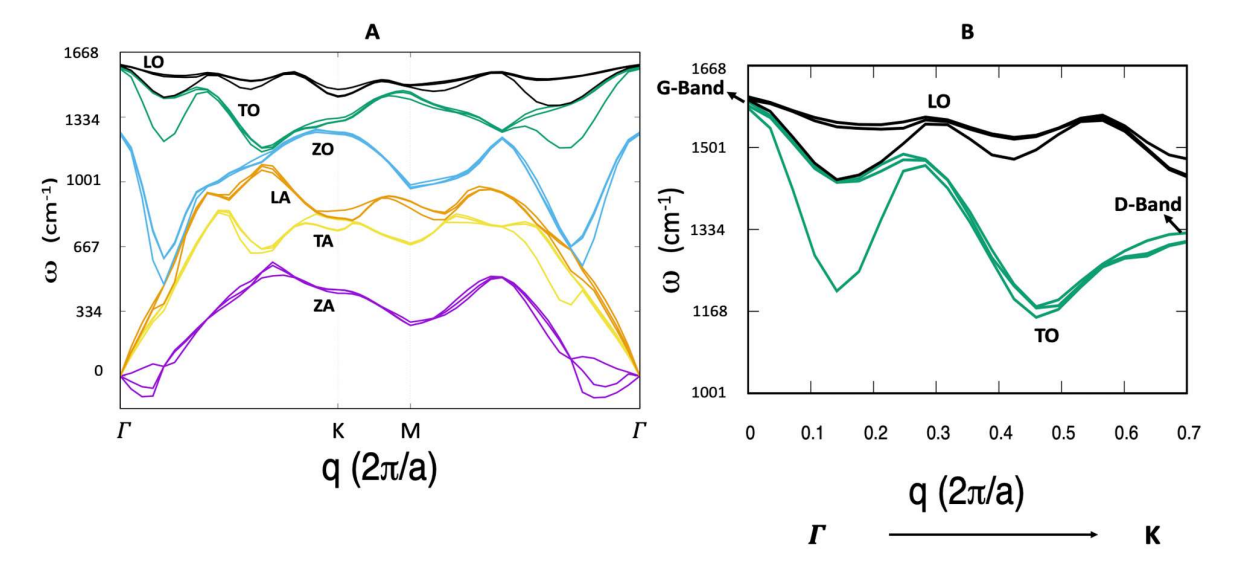


Figure 2. Calculated phonon dispersion relation of P-GnPs showing the (**A**) LO (black), TO (green), ZO (cyan), LA (orange), TA (yellow), and ZA (purple) phonon branches. (**B**) The LO (black) and TO (green) phonon branches are the only ones that contribute to the observed D, G, and 2D Raman peaks.

The phonon dispersion curves (LO, TO, ZO, LA, TA, and ZA) of trilayer graphene are plotted with respect to the Brillouin zone points (namely Γ , M, and K) and shown in Figure 2. However, emphasis is placed on the in-plane optical vibrational modes at the Γ and K points (LO and TO) shown in Figure 2B because they play a crucial role in studying the Raman spectra of P-GnPs. At the Γ -point, optical modes include the B_{2g} and E_{2g} vibrational modes, whereas the acoustic modes are composed of E_{1u} and A_{2u} modes. The E_{2g} doubly degenerate mode is Raman active. The E_{2g} mode at the Γ -point (TO + LO modes) and the A_{1g} mode at the K-point (TO mode) are the Raman G and D peaks, whose experimental data will be shown in a later section. The E_{2g} mode at the Γ -point of P-GnPs evolves into $E_{2g} = 2E_{2g} + E_{1u}$, while the A_{1g} mode at the K-point evolves into $A_{1g} = 2E + A_{1g}$ [15,16]. Frequencies of the various modes and their values, around both the G and K points, are provided in a later section.

2.2. Adsorption Simulations

The simulated untreated (P) GnP-based gas sensor consists of three parts: the substrates (Si/SiO₂), the electrodes (Au), and the active layer (P-GnPs with NO₂ and CO as target molecules). The detailed parameters of these elements are shown in Table 1, with many values being available in the public domain [17–22]. The base resistance of the untreated GnP-based sensor was determined via ambient air exposure, yielding a resistance of about $2.13 \times 10^3~\Omega$, well within reason for such a system [23]. Figure 3 shows the adsorption and desorption of NO₂ and air, respectively.

Data 2022, 7, 38 4 of 16

Table 1. Properties of the various elements of the simulated P-GnP-based sensor. Include	des references
for some of the values [21,22].	

Material	Width (m)	Length (m)	Thickness (m)	Electrical Conductivity (S/m)	Relative Permittivity
Si	9×10^{-3}	6×10^{-3}	1×10^{-3}	1×10^3	11.7
SiO ₂	9×10^{-3}	6×10^{-3}	3×10^{-5}	1×10^{-10}	3.9
Au	1.5×10^{-3}	1.7×10^{-3}	2×10^{-5}	5×10^7	6.9
P-GnPs	6.5×10^{-3}	6.0×10^{-3}	2×10^{-5}	766.87	37.9

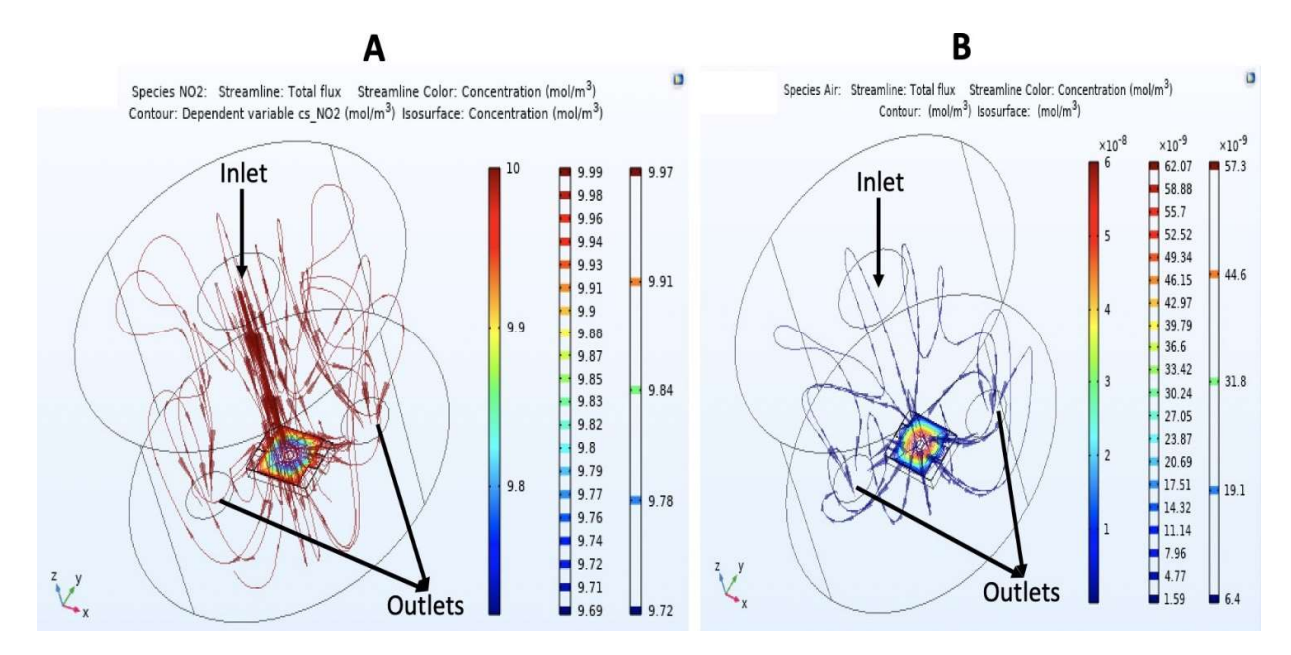


Figure 3. (**A**) Adsorption simulation involving NO₂. (**B**) Desorption of air from the surface of the simulated P-GnP-based gas sensor.

Figure 4 shows the resistance of the sensor exposed to NO_2 and CO, with concentrations varying between 10 mol/m³ and 70 mol/m³ at room temperature. When NO_2 , an oxidizing gas, is adsorbed on the surface of the P-GnPs, electrons are transferred to the gas, increasing the hole concentration in the P-GnPs and resulting in a resistance drop in the sensor. The simulation yields an opposite behavior for CO [24]. The initial resistance of the sensor is re-established after exposure to ambient atmospheric conditions.

The percent difference between the resistance of the sensor in air and that in the target gas is defined as the sensitivity of the sensor. The response and recovery cutoff times are defined by a threshold value of 90% of the corresponding equilibrium value after the target gas has been injected (or removed) from the chamber [25]. Time-dependent sensitivity data are presented in Figure 5, where the exposure gas concentration ranges from 10 mol/m^3 to 40 mol/m^3 . The sensor was predicted to achieve response and recovery times of about 10 s during such exposures.

Data 2022, 7, 38 5 of 16

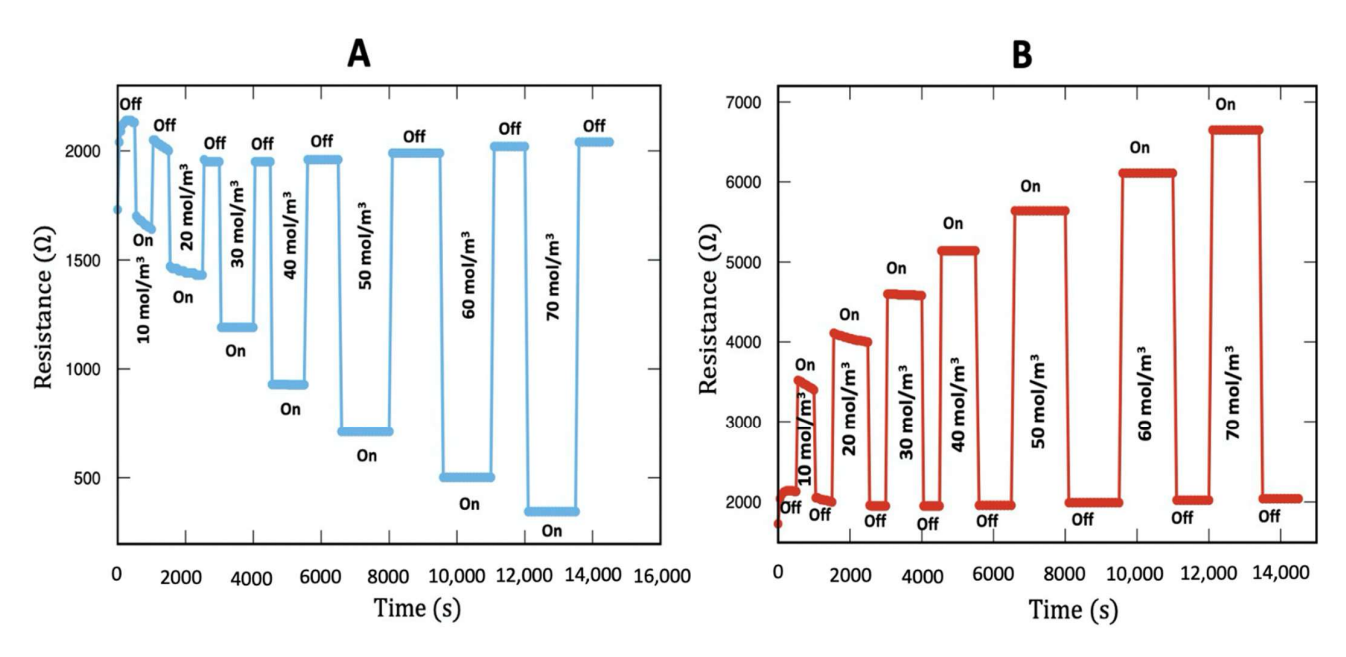


Figure 4. The time-dependent behavior of the resistance of the simulated P-GnP-based sensor at room temperature during exposure to (**A**) NO₂ and (**B**) CO.

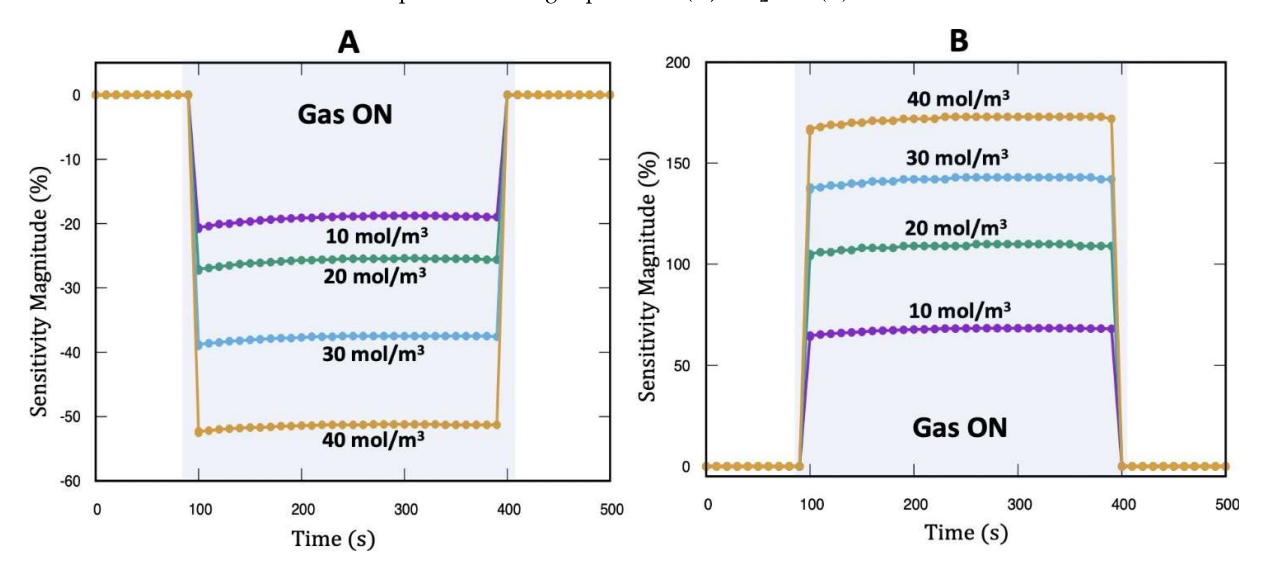


Figure 5. Response and recovery of the sensor as a function of time and concentration for **(A)** NO₂ and **(B)** CO at room temperature.

The sensitivity for each gas is also monitored as a function of concentration in Figure 6. As the concentration of NO_2 increased from 10 mol/m³ to 70 mol/m³, the sensitivity gradually increased from 23% to 84%, whereas the sensitivity for the CO case increased from 60% to 212%, indicating that CO is more reactive with the sensor.

Data 2022, 7, 38 6 of 16

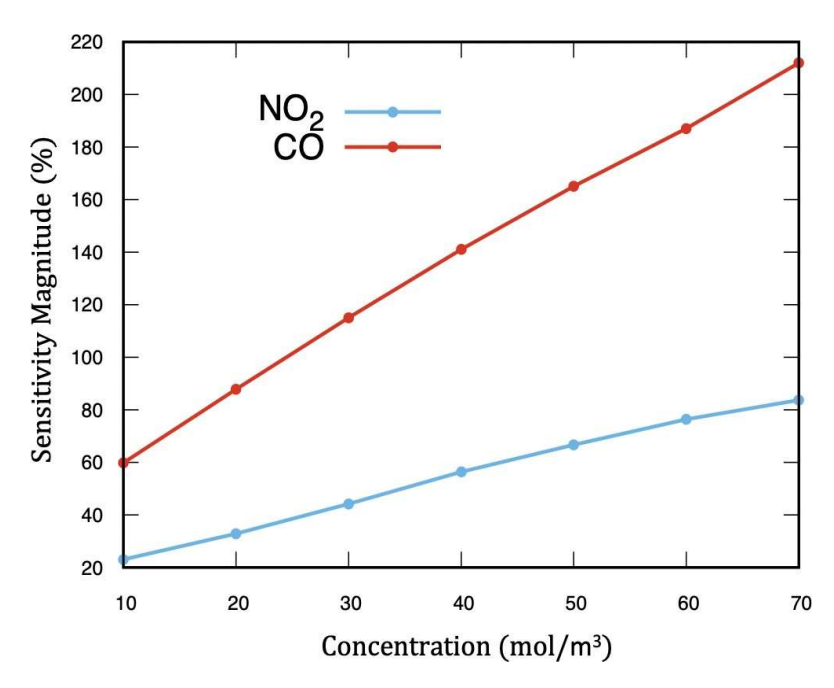


Figure 6. Sensitivity of simulated P-GnP-based sensors exposed to NO₂ and CO at room temperature.

Interactions between the NO₂ molecules and P-GnPs were turned on and the total system was equilibrated for 0.5 ns to adsorb the molecules. The number of adsorbed molecules were obtained by counting the number of molecules that are in a region of height 5 Å above the P-GnPs. The Lorentz–Bertholet combination rules ($\varepsilon_{ij} = \sqrt{\varepsilon_{ii}\varepsilon_{jj}}$ and $\sigma_{ij} = \frac{1}{2}(\sigma_{ii} + \sigma_{jj})$) were used to calculate the Lennard-Jones potential parameters describing interactions between the P-GnPs and NO₂. Nominally, ε_{ij} and σ_{ij} are the interaction energy and distance between particles i and j, respectively.

Finally, the adsorption energy is defined as $E_a = E_{bonded} - (E_{GnP-P} - E_{NO_2})$, where the first term is the total energy of the adsorbed system, the second term is the energy of P-GnP, and the last term is the energy of the NO₂ molecule. The adsorption energy of NO₂ on P-GnP was found to be about -35.5 kJ/mol (or -0.368 eV per molecule), with the negative value implying that adsorption has taken place and was an exothermic reaction. Also, our data show that 28 NO₂ molecules were adsorbed on the P-GnP sheet.

To get a better understanding of the observed adsorption properties, the Langmuir model is implemented for the case of NO_2 . The steady state solution for a single-species Langmuir model is

$$\theta_{i} = \frac{p_{i}}{p_{i} + P_{i (LD)} exp \left[\frac{-E_{i}}{k_{B}T}\right]} \tag{1}$$

The model in Equation (1) uses p as the partial pressure (with the fractional form multiplied by the total atmospheric pressure) of the gas species. If one defines $k_{\rm B}$ as the Boltzmann constant and T as the temperature (K), then the term $P_{(LD)}$ can denote the Langmuir desorption pressure, unique to each of the gas species, with the form

$$P_{LD} = \frac{k_{\rm B}T}{\left(\frac{h^2}{2\pi m k_{\rm B}T}\right)^{3/2}} \tag{2}$$

All parameters except for the partial pressure are approximately known, so to estimate the latter, the concentration may be converted by comparing the number of particles of NO_2 with those from the constituents of air. Doing this for 10 mol/m^3 gives a partial pressure fraction of about 0.18 (assuming standard temperature and pressure at 101,325 Pa). With

Data 2022, 7, 38 7 of 16

all of these components known and used in Equation (1), there is an approximate coverage of 2.2%.

2.3. Diagnostic Electrical Measurement

The I–V characteristics of the P-GnP samples were determined within the range of -0.1 V to 0.1 V at room temperature. These data are shown in Figure 7. The average resistance of the P-GnPs was found to be 0.2Ω , yielding a conductivity of about 766.87 S/m.

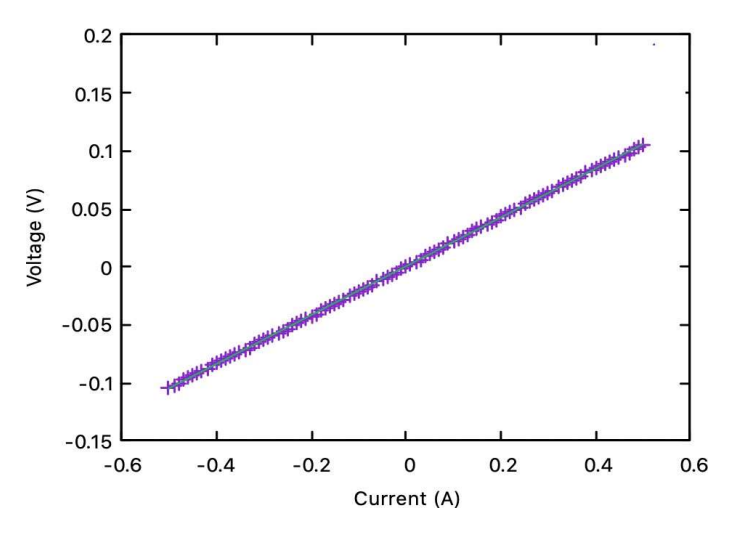


Figure 7. Current-voltage characteristics of P-GnPs.

2.4. Morphology of Untreated and Chemically Treated GnPs

SEM images were obtained and are shown in Figure 8 [26,27] $^{\partial}$. The SEM images of P-GnPs show that the platelets are randomly stacked on each other, forming aggregates, a behavior that suggests a strong hydrophobicity and van der Waals interaction.

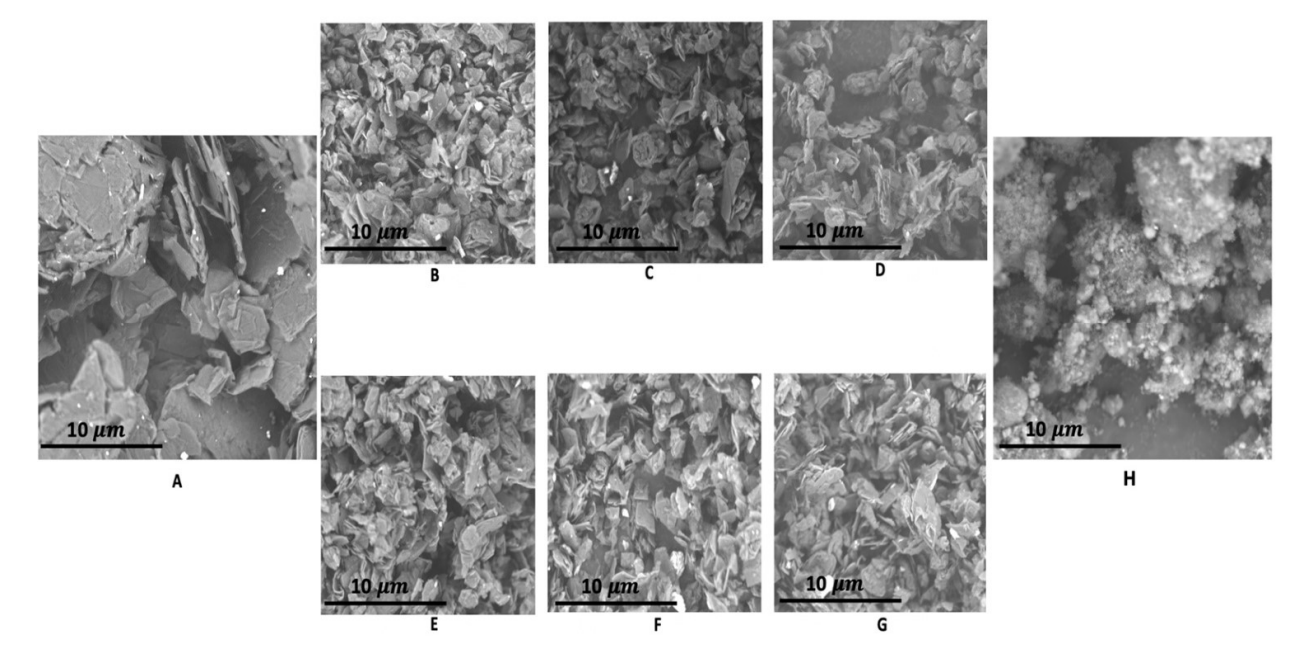


Figure 8. SEM images are shown for **(A)** P-GnPs, **(B)** GnPs-NH3, **(C)** GnPs-A, **(D)** GnPs-COOH, **(E)** GnPs-CF, **(F)** GnPs-N, **(G)** GnPs-O, and **(H)** GnPs-35COOH. All images have a 10 µm scale bar.

Data 2022, 7, 38 8 of 16

It was observed that, when compared with P-GnPs, the chemically treated GnPs were generally fragmented and of smaller lateral sizes, which can be attributed to the dielectric barrier discharge plasma method employed in the synthesis of the chemically treated samples [28]. For instance, during graphene oxide (GO) synthesis, research has shown that acids and oxidizing agents can break the GO sheets into smaller lateral sizes when exposed for a long oxidation time [29,30]. The SEM image of the GnPs-35COOH shows that the platelets become smaller to form conglomerates, and this lateral shrinking may be attributable to the edges becoming delaminated as well as a sufficiently high concentration of oxygen-containing functional groups in the sample.

2.5. Raman Spectra of Untreated and Chemically Treated GnPs

The vibrational properties of untreated and chemically treated GnPs were investigated by Raman spectroscopy. Three major peaks and one minor peak were observed in the Raman spectra of the untreated and chemically treated GnP samples shown in Figure 9, namely the D peak (between 1349 cm $^{-1}$ and 1357 cm $^{-1}$), which indicates the presence of disorder in the sp 2 -bonded carbon lattice [31]; the G peak (between 1580 cm $^{-1}$ and 1583 cm $^{-1}$), attributed to the in-plane stretching vibration of the sp 2 bonded carbon atoms [32]; the 2D peak (between 2707 cm $^{-1}$ and 2723 cm $^{-1}$), which originates from the combination of two Raman A_{1g} modes; and lastly the 2D′ peak, representing a second order mode of the D′ peak [33]. The Raman spectra of GnPs-COOH, GnPs-35COOH, GnPs-A, GnPs-NH₃, GnPs-N, GnPs-O, and GnPs-CF show an increase in the D band intensities compared to P-GnPs, indicating the formation of defects in the structures. In addition, the observed D′ peak in all chemically treated GnP samples′ spectra may be attributed to the presence of the functional groups introduced and is activated by two-phonon double resonance Raman scattering involving one longitudinal optical (LO) phonon near the gamma (Γ) point [34].

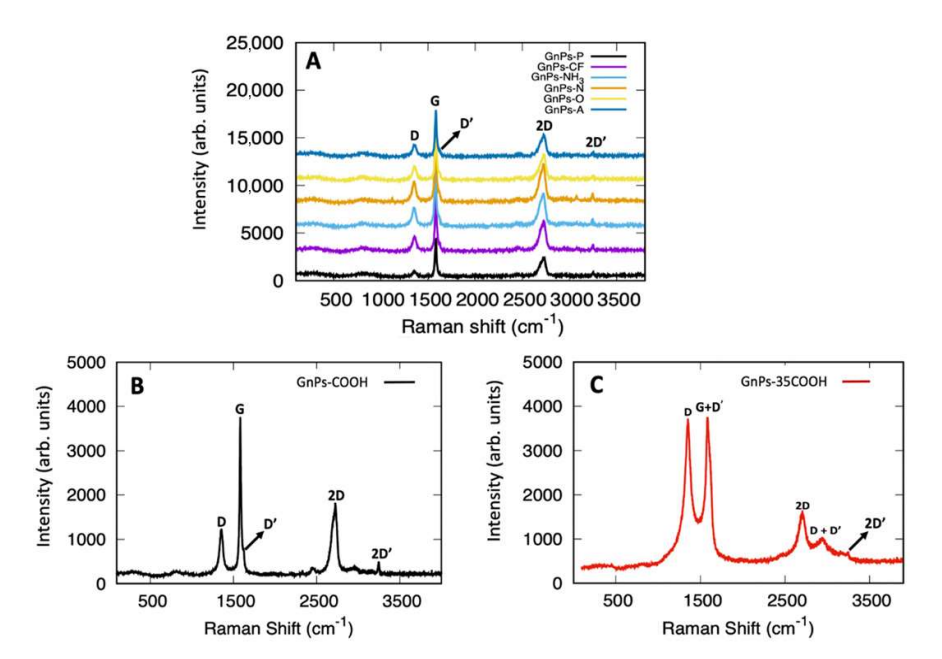


Figure 9. Raman spectra are shown for **(A)** GnPs-A (blue), GnPs-O (yellow), GnPs-N (orange), GnPs-NH3 (cyan), GnPs-CF (purple), and P-GnPs (black). The D, G, D', 2D, and 2D' peaks are labeled as such. **(B)** Raman spectrum shown for GnPs-COOH. **(C)** Raman spectrum shown for GnPs-35COOH, with additional labels for the D + D' peak. Note the ratio ID/IG is nearly unity, a feature not seen with other chemically treated GnPs, but this may be because of differences in product quality.

However, the D' peak merges with the G peak, forming the G + D' in the Raman spectrum of GnPs-35COOH as shown in Figure 9c. This is because of the G-band peak broadening, indicating a higher degree of disorder in the structure compared to the low

Data 2022, 7, 38 9 of 16

density chemically treated GnP samples. The Raman spectrum of GnPs-35COOH is characterized by intense D and broad 2D peaks. The increase in intensity of the D peak of GnPs-35COOH in relation to the D peak of the GnPs with low density chemical treatment indicates an increase in the amount of the structural disorder. Also, the appearance of the D + D' peak in the GnPs-35COOH spectrum could indicate more $\rm sp^3$ -hybridized carbon relative to $\rm sp^2$ -hybridezed carbon.

One consequence of doping with the functional groups is that a significant increase in the average value of I_D/I_G occurs with respect to the concentration of doping introduced as shown in Table 2. This phenomenon could be one reason GnPs-35COOH has the highest I_D/I_G average value (about 0.93, nearly 3 times as high as the other species' values). The I_D/I_G average values of the low density chemically treated GnPs change by a small amount (i.e., from about 0.25 for untreated to roughly 0.3-0.35 for most of these species). The most significant change was observed in the I_D/I_G average of GnPs-35COOH, which was about 0.93. This ratio change indicates that the carboxyl group introduces electron doping to untreated GnPs [35,36]. A significant Raman shift is not observed in the G peak frequency of all the chemically treated GnP samples, indicating the functional groups introduced are not causing a significant amount of strain within the structure. As seen in Figure 9c, there is an observable redshift in the 2D peak frequency of GnPs-35COOH which again confirms the introduction of electron doping when carboxyl is introduced. The frequency of the 2D band is expected to shift to lower frequencies upon *n*-type doping in graphene based on earlier research studies [37,38]. Also, a slight decrease in the I_{2D}/I_G value of GnPs-35COOH was observed, which confirms the *n*-type behavior of GnPs-35COOH [35].

Table 2. The average intensity ratios of D and G (I_D/I_G), 2D and G (I_{2D}/I_G) peaks and Raman positions of the D, G, and 2D peaks for untreated and chemically treated GnPs.

Samples	Band D (cm^{-1})	Band G (cm ⁻¹)	Band 2D (cm ⁻¹)	I_D/I_G	I_{2D}/I_{G}
GnPs-P	1354 ± 3.3	1581 ± 1.1	2722 ± 2.5	0.25 ± 0.10	0.58 ± 0.10
GnPs-NH ₃	1355 ± 2.2	1582 ± 1.4	2722 ± 2.3	0.36 ± 0.01	0.51 ± 0.05
GnPs-A	1356 ± 2.2	1583 ± 0.2	2723 ± 1.4	0.34 ± 0.01	0.53 ± 0.03
GnPs-COOH	1354 ± 2.0	1581 ± 1.7	2721 ± 3.7	0.33 ± 0.03	0.52 ± 0.03
GnPs-35COOH	1350 ± 5.4	1581 ± 1.8	2708 ± 5.4	0.93 ± 0.04	0.41 ± 0.04
GnPs-CF	1356 ± 1.4	1582 ± 0.7	2723 ± 3.3	0.29 ± 0.02	0.50 ± 0.07
GnPs-N	1355 ± 1.0	1581 ± 0.9	2720 ± 1.0	0.36 ± 0.03	0.50 ± 0.02
GnPs-O	1357 ± 0.6	1583 ± 0.3	2724 ± 1.7	0.32 ± 0.01	0.52 ± 0.02

2.6. X-ray Photoelectron Spectra of Untreated and Chemically Treated GnPs

The surface composition of the untreated and chemically treated GnPs was analyzed using XPS. As an example, Figure 10 gives the high-resolution C 1s, O 1s, N 1s, and F 1s spectra for a dozen different samples acquired from three distinct vendors, as summarized in Tables 3 and 4. The C 1s spectra are fit with peaks corresponding to the following bonding environments: C=C (sp²-bonded carbon atoms), C-C (sp³-bonded carbon atoms), C=O (carbonyl), C-N, C-O, and C-F. A pi-pi* shake-up peak is also visible. These data give a general assessment of the quality of the materials, with some of the treatments being directly comparable, such as the oxygen-, carboxyl-, and ammonia-treated GnPs. We may conclusively say that some forms of treatment result in compositions that are up to an order of magnitude different, judging by the total counts for certain bonds. These data also provide verification of the valuable information attainable with this spectroscopy, namely the composition information and bonding types. The O 1s peak is particularly large (by up to an order of magnitude stronger) for the carboxyl 35% treated samples compared with the other chemically treated GnPs [39].

Data 2022, 7, 38 10 of 16

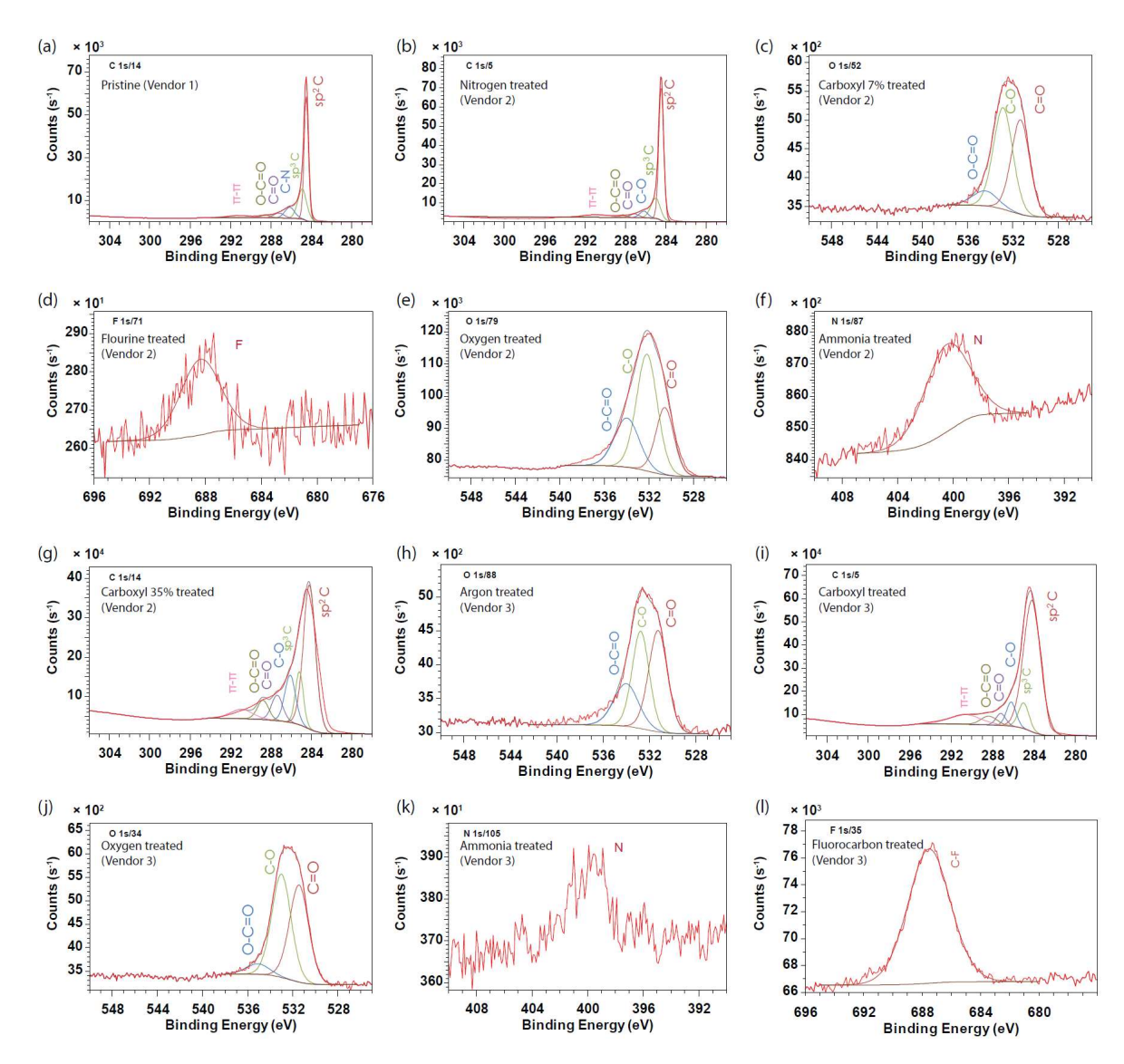


Figure 10. XPS spectra of a dozen different samples whose ranges were selected based on the type of chemical treatment performed. There are twelve distinct GnP types from three different vendors (as labeled in the corresponding tables) with the following treatments: (a) pristine (b) nitrogen, (c) carboxyl (7%), (d) fluorine, (e) oxygen, (f) ammonia, (g) carboxyl (35%), (h) argon, (i) carboxyl, (j) oxygen (different vendor), (k) ammonia (different vendor), and (l) fluorocarbon.

Table 3. Tabulated composition percentages determined from XPS spectra of materials acquired from Vendor 1.

Percentage Compositions for Vendor 1 (US Research Nanomaterials)				
Untreated GnP				
51.2				
25.6				
10.2				
4.9				
2.5				
2.4				
3.2				

Data 2022, 7, 38 11 of 16

Table 4. Tabulated composition percentages from XPS spectra of materials acquired from Vendors 2 and 3. Prominent or treatment-specific elements are examined with XPS in Figure 10.

Percentage Compositions for Vendor 2 (Cheaptubes)							
Component	Nitrogen Treated	Carboxyl (7%) Treated	Fluorine Treated	Oxygen Treated	Ammonia Treated	Carboxyl (35%) Treated	
sp ² C	65.9	62.3	68.3	56.8	55.1	46.7	
sp ³ C	19.7	20.2	14.2	17	19.3	11.3	
C-O	5.6	8.6	8	12.3	12.7	13.7	
C=O	3.4	3.2	3.2	5.9	5.6	7.7	
O-C=O	1.6	2	2	3.3	2.9	5.9	
O 1s	3.7	3.7	3.8	3.8	3.6	13.8	
F 1s	-	-	0.6	-	-	-	
N 1s	trace	trace	-	0.9	0.7	1	

Percentage Compositions for Vendor 3 (Graphene Supermarket)

		<i>3</i> 1		1 1		
Component	Argon Treated	Carboxyl Treated	Oxygen Treated	Nitrogen Treated	Ammonia Treated	Fluorocarbon Treated
sp ² C	66	68.4	64	67.6	67.6	72.6
sp ³ C	17.6	8	21.5	15.7	14	6
C-O	7.1	8.5	4.3	7.5	6.3	6.8
C=O	3	5.3	4	3.1	6.1	4.9
O-C=O	2.3	5.4	1.3	1.9	2.3	3.2
C-F	_	-	_	-	-	2
O 1s	4	4.3	4.8	4.2	3.7	3.4
F 1s	_	_	_	trace	-	1.1
N 1s	-	trace	-	trace	trace	_

2.7. X-ray Diffraction Spectra of Untreated and Chemically Treated GnPs

The structural quality of untreated and chemically treated GnPs was determined by XRD. The (002), (100), (004), (221), and (110) reflections were observed in the XRD patterns of P-GnPs, GnPs-COOH, GnPs-A, GnPs-NH₃, GnPs-N, GnPs-O, and GnPs-CF shown in Figure 11, where each of the peaks represents the planes in the hexagonal crystal lattice of GnPs. The high intensity peak found at 38° 20 is from the powder sample holder in the Thermo Scientific X-ray diffractometer utilized in collecting the spectra. The high intensity (002) reflection found between 26.36° 20 and 26.71° 20 in the XRD pattern of P-GnPs, GnPs-COOH, GnPs-A, GnPs-NH₃, GnPs-O, GnPs-N, and GnPs-CF confirms a high degree of crystallinity of the samples [40]. The (002) reflections of the untreated and chemically treated GnP samples correspond to an interlayer spacing (d_{002}) of 0.34 nm which was calculated using Bragg's formula; the value was found to agree well with the d_{002} value of graphite [18]. This result suggests that the functional groups present do not cause significant strain within the structure or lattice expansion.

$$d_{002} = \frac{n\lambda}{\sin\,\theta} \tag{3}$$

Data 2022, 7, 38 12 of 16

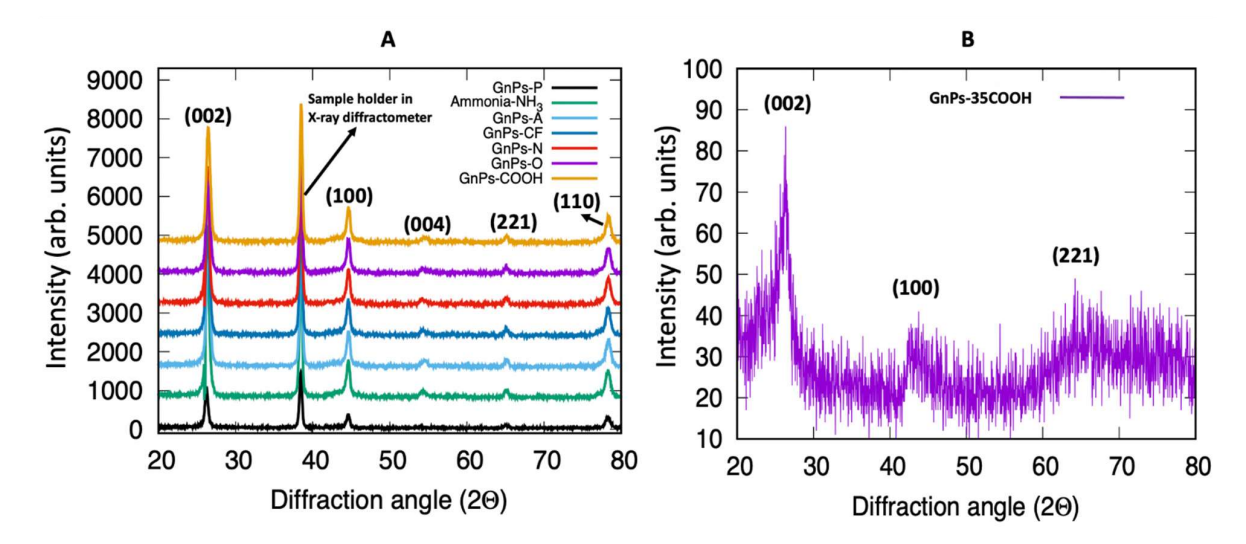


Figure 11. XRD spectra are shown for (**A**) P-GnPs (black), GnPs-NH3 (green), GnPs-A (cyan), GnPs-CF (blue), GnPs-N (red), GnPs-O (purple), and GnPs-COOH (orange). The various diffraction peaks are labeled accordingly. (**B**) The weaker XRD signal warranted a separate analysis of the GnPs-35COOH.

However, the XRD spectra of GnPs-35COOH show a lower intensity and broader peaks, indicating a low structural quality and highly disordered GnP sheets. The in-plane (L_a) and out-of-plane distances along the c-direction (L_c) , and other relevant length scales are shown in Table 5. Based on the (100) peak, the approximate lattice constant (a) was calculated to be around 0.23 nm, which is slightly smaller than the typically reported value. This may be due to the slightly higher diffraction angle observed here and reflects possible errors from calibration. Based on the (002) peak, the corresponding lattice constant c was calculated to be 0.67 nm, much closer to the widely accepted value. This leads to a unit cell volume of about 0.0306 nm³. It is important to note that this corresponds most closely to graphite, indicating that the crystallites are still bonded by van der Waals forces. Some values were calculated from the full width half maximum (FWHM) values of the (100) and (002) peaks using the Scherrer equation [41]. The data show that the crystallite sizes of the chemically treated GnP samples became smaller, which agrees with the SEM data presented earlier. Also, GnPs-35COOH was observed to have a smaller crystallite size compared to the GnPs-COOH, GnPs-A, GnPs-NH₃, GnPs-O, GnPs-N, and GnPs-CF samples, suggesting a distortion or delamination of the edges to a large extent. Table 5 also displays the overall number of layers along the c-direction (N_c) [42] in the GnPs' aggregates, calculated using the relation $N_c = \frac{L_c}{d_{002}}$. The data show that GnPs-35COOH have the lowest number of layers, demonstrating a high degree of exfoliation from graphite. Though the exact nature of the defect sites on the GnP surfaces are not exactly determinable with these methods, one could employ the following techniques to determine this: high resolution transmission electron microscopy and a volumetric adsorption system.

Data 2022, 7, 38 13 of 16

Table 5. The crystallographic reflections, corresponding full-width at half-maxima (FWHM), interlayer distance (d), out-of-plane crystallite sizes (L_c), in-plane crystallite sizes (L_a), and number of layers (N_c) are tabulated for P-GnPs, GnPs-COOH, GnPs-35COOH, GnPs-NH3, GnPs-O, GnPs-N, GnPs-A, and GnPs-CF.

Samples	(20)° (002)	FWHM (002) (2θ)°	(20)° (100)	FWHM (100) (2θ)°	d ₀₀₂ (nm)	L _c (nm)	L _a (nm)	N _C
GnPs-P	26.50	0.4734	44.56	1.0986	0.3360	17.05	7.73	51
GnPs-NH ₃	26.54	0.8367	44.64	3.2530	0.3356	9.65	2.61	29
GnPs-A	26.71	0.5326	44.63	4.0596	0.3350	15.15	2.09	45
GnPs-COOH	26.54	0.6214	44.63	4.3000	0.3356	13.04	1.98	39
GnPs-35COOH	26.36	2.5200	43.76	5.31	0.3378	3.200	1.59	9
GnPs-CF	26.54	0.6214	44.63	3.6255	0.3356	13.04	2.34	39
GnPs-N	26.37	0.5030	44.58	3.7426	0.3376	16.00	2.27	47
GnPs-O	26.36	0.6806	44.66	4.9943	0.3376	11.83	1.7	35

3. Methods

Regarding the simulations, both COMSOL software and the Large-scale Atomic/Molecular Massively Parallel Simulator (LAMMPS (Release stable 29 September 2021 update 3)) software package from Sandia National Laboratories [15] were used. $^{\partial}$ The computed dynamical matrices are then passed to a post-processing code to evaluate the vibrational properties.

$$D_{k \propto k' \beta}(q) = \frac{1}{\sqrt{m_k m_{k'}}} \phi_{k \propto k' \beta}(q) \tag{4}$$

where $\phi_{k\infty,k'\beta}(q)$ is the force constant coefficient of the system in reciprocal space. LAMMPS is a MD simulation software code that can model micro-canonical (NVE, meaning constant energy and constant volume), canonical (NVT, meaning constant volume and constant temperature), and grand-canonical ensembles of a system of particles in liquid, solid, or gaseous state using a variety of fields, potentials, and boundary conditions [16].

Simulations were carried out on trilayer graphene using the optimized Tersoff and Brenner empirical interatomic potential to describe the interactions between the carbon atoms [17]. The trilayer graphene model represents one pure (untreated) platelet in our GnPs' aggregates (P-GnPs), where one flake consists of a short stack of three to six layers of graphene. The theoretical lattice constant (a^{theor.}) of trilayer graphene was calculated to be 2.4856 Å using the optimized Tersoff and Brenner empirical potential, which agrees well with the experimental lattice constant of graphene, 2.46 Å [18]. The lengths of the simulation box used in the x and y directions are $L_X = 24.85$ Å and $L_Y = 21.52$ Å, with a vacuum region of 35 Å applied in the z direction to avoid interaction between the periodic images. A time step of 0.002 ps was used during the micro canonical ensemble simulation (NVE) for proper equilibration of the system with a total run time of 16 ns. Periodic boundary conditions are employed in the x, y, and z directions to eliminate boundary effects caused by finite system size.

For the case of COMSOL simulations, the boundary conditions for the entry and exit of NO_2 and CO molecules are defined as "no slip" (gas velocity is zero at the container edges). The normal flow velocity was defined for NO_2 and CO molecules at the inlet $(U_{inlet}=0.05~\text{m/s})$. The boundary conditions for adsorption are such that the mass of the NO_2 and CO molecules is conserved within the simulation region, though some of the mass may be distributed in the bulk and on the surface. Additionally, the adsorption and desorption processes are subject to constraints of both the Navier–Stokes equation and the convection–diffusion equation.

Data 2022, 7, 38 14 of 16

A cylindrical chamber of diameter and height, d = h = 0.02 m, was designed to contain the environment in which the sensor is exposed to NO_2 and CO gases. The chamber has two outlets of radius r = 0.003 m, each located at the bottom of the chamber, and also has one inlet of radius r = 0.005 m, located at the top of the chamber. The inlet serves as an entry point for the gases, whereas the two smaller outlets serve as an exit point for the gases. The sensor was placed in the middle of the chamber to allow for uniform adsorption.

The adsorption properties of NO₂ on P-GnPs (consisting of three graphene layers) were investigated using MD simulations within the LAMMPS software code. A simulation space was given dimensions of 24.9 Å \times 21.5 Å \times 60 Å in the x, y, and z directions, respectively. The P-GnPs was placed at the bottom of the box and the boundary conditions were set to be periodic in all directions. Fifty NO₂ molecules were randomly deposited inside the simulation space and energy minimization was performed to relax the P-GnP sheet. Equilibration of the NO₂ molecules only was then carried out using the canonical ensemble (NVT) to uniformly distribute the molecules for 0.1 ns.

For the electrical characterization, four trials of current-voltage (I–V) measurements were taken using the Alessi REL-4100A analytical probe station with 1 μ m resolution in all directions. $^{\vartheta}$ Electrical probes were directly injected into compressed pucks composed of P-GnPs to allow for the application of electrical current.

The untreated GnPs were acquired from US Research Nanomaterials, Inc., $^{\vartheta}$ whereas GnPs chemically treated with low-density ammonia, carboxyl, argon, nitrogen, oxygen, and fluorocarbon functional groups were acquired from Graphene Supermarket. $^{\vartheta}$ GnPs treated with nitrogen, carboxyl (7%), fluorine, oxygen, ammonia, and 35% (by weight) carboxyl were acquired from Cheap Tubes, Inc. $^{\vartheta}$ No chemical alterations or modifications were imposed on the acquired samples.

The scanning electron microscope (SEM) gave information about the morphology of all GnP species. The Phenom Pure SEM $^{\vartheta}$ was used with a magnification that ranges from $20\times$ to $65,000\times$.

Raman spectroscopy data were recorded on a Renishaw inVia Raman spectrometer using a 514 nm wavelength excitation laser source, a laser beam quality of 0.65 mm, and a laser maximum power of 50 mW. 9 The spectra were collected using a laser exposure time of 10 s with 10 accumulations to reduce the signal-to-noise ratio.

The XRD spectra of P-GnPs, GnPs-NH₃, GnPs-COOH, GnPs-A, GnPs-N, GnPs-O, and GnPs-CF were collected using the Thermo Scientific ARL EQUINOX 100 X-Ray diffractometer $^{\partial}$ with Cu K $_{\infty}$ radiation, whereas the XRD spectrum of GnPs-35COOH was collected using the Philips X'Pert powder X-ray diffractometer, also with Cu K $_{\infty}$ radiation $^{\partial}$.

XPS measurements were performed using the Kratos Axis Ultra X-ray photoelectron spectrometer operating at a base pressure of about 2.66×10^{-7} Pa (about 2×10^{-9} Torr). $^{\partial}$ All samples were analyzed using monochromatic Al K_{∞} (1486.7 eV) with a spot size of 300 $\mu m \times 700~\mu m$. Pass energies of 160 eV and 20 eV were used to collect the survey and high-resolution core level XPS spectra, respectively. All experimental uncertainties (1 σ) arise from the uncertainty of the instrumentation used for this work.

Author Contributions: O.Z.F.: Conceptualization, methodology, software, validation, formal analysis, writing—original draft, visualization. H.A.: Conceptualization, validation, formal analysis, writing—original draft. S.M.M.: Validation, writing—original draft. M.L.K.: Validation, writing—original draft. A.V.D.: Validation, writing—original draft, supervision. C.A.H.: Validation, writing—original draft, supervision. A.F.R.: Validation, writing—original draft, supervision. All authors have read and agreed to the published version of the manuscript.

Funding: This research was funded by the National Science Foundation under grant numbers PHY 1950379, DMR 2101121, TG-DMR190126, and TG-PHY210066. The APC was funded by the same. Some of the work presented herein was performed, for a subset of the authors, as part of their official duties for the United States Government. Funding is hence appropriated by the United States Congress directly.

Data 2022, 7, 38 15 of 16

Informed Consent Statement: Not applicable.

Data Availability Statement: Data available upon request to the corresponding author.

Acknowledgments: P.M. would like to acknowledge the financial support from the National Science Foundation REU Site in Physics at Howard University (NSF Award No. PHY 1950379) and Excellence in Research (NSF Award No. DMR 2101121), and allocation support from the Extreme Science and Engineering Discovery Environment (XSEDE Grant Nos. TG-DMR190126 and TG-PHY210066). M.K. acknowledges support from the National Institute of Standards and Technology (NIST) Financial Assistance Award with Federal Award ID 70NANB19H152.

Conflicts of Interest: The authors declare no conflict of interest.

References

- 1. Mittal, M.; Kumar, A. Carbon nanotube (CNT) gas sensors for emissions from fossil fuel burning. *Sens. Actuators B Chem.* **2014**, 203, 349–362. [CrossRef]
- 2. Han, T.; Nag, A.; Mukhopadhyay, S.C.; Xu, Y. Carbon nanotubes and its gas-sensing applications: A review. *Sens. Actuators A Phys.* **2019**, 291, 107–143. [CrossRef]
- 3. Tian, W.; Liu, X.; Yu, W. Research progress of gas sensor based on graphene and its derivatives: A review. *Appl. Sci.* **2018**, *8*, 1118. [CrossRef]
- 4. Yang, S.; Jiang, C.; Wei, S. Gas sensing in 2D materials. Appl. Phys. Rev. 2017, 4, 021304. [CrossRef]
- 5. Kalaitzidou, K.; Fukushima, H.; Drzal, L.T. Multifunctional polypropylene composites produced by incorporation of exfoliated graphite nanoplatelets. *Carbon* **2007**, *45*, 1446–1452. [CrossRef]
- 6. Kim, S.; Do, I.; Drzal, L.T. Multifunctional xGnP/LLDPE nanocomposites prepared by solution compounding using various screw rotating systems. *Macromol. Mater. Eng.* **2009**, 294, 196–205. [CrossRef]
- 7. Hu, J.; Rigosi, A.F.; Lee, J.U.; Lee, H.Y.; Yang, Y.; Liu, C.I.; Elmquist, R.E.; Newell, D.B. Quantum transport in graphene p—n junctions with moiré superlattice modulation. *Phys. Rev. B* **2018**, *98*, 045412. [CrossRef]
- 8. Rigosi, A.F.; Hill, H.M.; Glavin, N.R.; Pookpanratana, S.J.; Yang, Y.; Boosalis, A.G.; Hu, J.; Rice, A.; Allerman, A.A.; Nguyen, N.V.; et al. Measuring the dielectric and optical response of millimeter-scale amorphous and hexagonal boron nitride films grown on epitaxial graphene. 2D Mater. 2017, 5, 011011. [CrossRef]
- 9. Oe, T.; Rigosi, A.F.; Kruskopf, M.; Wu, B.Y.; Lee, H.Y.; Yang, Y.; Elmquist, R.E.; Kaneko, N.H.; Jarrett, D.G. Comparison between NIST graphene and AIST GaAs quantized Hall devices. *IEEE Trans. Instrum. Meas.* **2019**, *69*, 3103–3108. [CrossRef]
- 10. Ponzoni, A.; Baratto, C.; Cattabiani, N.; Falasconi, M.; Galstyan, V.; Nunez-Carmona, E.; Rigoni, F.; Sberveglieri, V.; Zambotti, G.; Zappa, D. Metal oxide gas sensors, a survey of selectivity issues addressed at the SENSOR Lab, Brescia (Italy). *Sensors* **2017**, *17*, 714. [CrossRef]
- 11. Wu, Z.; Chen, X.; Zhu, S.; Zhou, Z.; Yao, Y.; Quan, W.; Liu, B. Enhanced sensitivity of ammonia sensor using graphene/polyaniline nanocomposite. *Sens. Actuators B Chem.* **2013**, *178*, 485–493. [CrossRef]
- 12. Pinelli, F.; Nespoli, T.; Fiorati, A.; Farè, S.; Magagnin, L.; Rossi, F. Graphene nanoplatelets can improve the performances of graphene oxide–polyaniline composite gas sensing aerogels. *Carbon Trends* **2021**, *5*, 100123. [CrossRef]
- 13. Zhang, R.; Jia, J.B.; Cao, J.L.; Wang, Y. SnO₂/Graphene Nanoplatelet Nanocomposites: Solid-State Method Synthesis With High Ethanol Gas-Sensing Performance. *Front. Chem.* **2018**, *6*, 337. [CrossRef] [PubMed]
- 14. Kong, L.T. Phonon dispersion measured directly from molecular dynamics simulations. *Comput. Phys. Commun.* **2011**, *182*, 2201–2207. [CrossRef]
- 15. Yan, J.A.; Ruan, W.Y.; Chou, M.Y. Phonon dispersions and vibrational properties of monolayer, bilayer, and trilayer graphene: Density-functional perturbation theory. *Phys. Rev. B* **2008**, 77, 125401. [CrossRef]
- 16. Lan, Y.; Zondode, M.; Deng, H.; Yan, J.-A.; Ndaw, M.; Lisfi, A.; Wang, C.; Pan, Y.-L. Basic concepts and recent advances of crystallographic orientation determination of graphene by Raman spectroscopy. *Crystals* **2018**, *8*, 375. [CrossRef]
- 17. Large-Scale Atomic and Molecular Massively Parallel Simulator, "Lammps". Available online: http://lammps.sandia.gov (accessed on 1 November 2021).
- 18. Plimpton, S. Fast parallel algorithms for short-range molecular dynamics. J. Comput. Phys. 1995, 117, 1–19. [CrossRef]
- 19. Lindsay, L.; Broido, D.A. Optimized Tersoff and Brenner empirical potential parameters for lattice dynamics and phonon thermal transport in carbon nanotubes and graphene. *Phys. Rev. B* **2010**, *81*, 205441. [CrossRef]
- 20. Mohr, M.; Maultzsch, J.; Dobardžić, E.; Reich, S.; Milošević, I.; Damnjanović, M.; Bosak, A.; Krisch, M.; Thomsen, C. Phonon dispersion of graphite by inelastic x-ray scattering. *Phys. Rev. B* **2007**, *76*, 035439. [CrossRef]
- 21. Shklyarevskii, I.N.; Pakhomov, P.L. Separation of contributions from free and cou-pled electrons into real and imaginary parts of a dielectric-constant of gold. *Opt. Spektrosk.* **1973**, 34, 163–166.
- 22. Wang, A.; Chung, D.D.L. Dielectric and electrical conduction behavior of carbon paste electrochemical electrodes, with decoupling of carbon, electrolyte and interface contributions. *Carbon* **2014**, *72*, 135–151. [CrossRef]
- 23. Davaji, B.; Cho, H.D.; Malakoutian, M.; Lee, J.K.; Panin, G.; Kang, T.W.; Lee, C.H. A patterned single layer graphene resistance temperature sensor. *Sci. Rep.* **2017**, *7*, 8811.

Data **2022**, 7, 38 16 of 16

24. Tang, X.; Debliquy, M.; Lahem, D.; Yan, Y.; Raskin, J.P. A review on functionalized graphene sensors for detection of ammonia. Sensors 2021, 21, 1443. [CrossRef]

- 25. Utari, L.; Septiani, N.L.W.; Nur, L.O.; Wasisto, H.S.; Yuliarto, B. Wearable carbon monoxide sensors based on hybrid graphene/zno nanocomposites. *IEEE Access* **2020**, *8*, 49169–49179. [CrossRef]
- 26. Nečas, D.; Klapetek, P. Gwyddion: An open-source software for SPM data analysis. Open Phys. 2012, 10, 181–188. [CrossRef]
- 27. Hill, H.M.; Rigosi, A.F.; Chowdhury, S.; Yang, Y.; Nguyen, N.V.; Tavazza, F.; Elmquist, R.E.; Newel, D.B.; Walker, A.R.H. Probing the dielectric response of the interfacial buffer layer in epitaxial graphene via optical spectroscopy. *Phys. Rev. B* **2017**, *96*, 195437. [CrossRef] [PubMed]
- 28. Brković, D.V.; Kovačević, V.V.; Sretenović, G.B.; Kuraica, M.M.; Trišović, N.P.; Valentini, L.; Marinković, A.D.; Kenny, J.M.; Uskoković, P.S. Effects of dielectric barrier discharge in air on morphological and electrical properties of graphene nanoplatelets and multi-walled carbon nanotubes. *J. Phys. Chem. Solids* **2014**, *75*, 858–868. [CrossRef]
- 29. Shojaeenezhad, S.S.; Farbod, M.; Kazeminezhad, I. Effects of initial graphite particle size and shape on oxidation time in graphene oxide prepared by Hummers' method. *J. Sci.* **2017**, *2*, 470–475. [CrossRef]
- 30. Jeon, I.Y.; Choi, H.J.; Jung, S.M.; Seo, J.M.; Kim, M.J.; Dai, L.; Baek, J.B. Large-scale production of edge-selectively functionalized graphene nanoplatelets via ball milling and their use as metal-free electrocatalysts for oxygen reduction reaction. *J. Am. Chem. Soc.* 2013, 135, 1386–1393. [CrossRef]
- 31. Sfyris, D.; Sfyris, G.I.; Galiotis, C. Stress intrepretation of graphene E-2g and A-1g vibrational modes: Theoretical analysis. *arXiv* **2017**, arXiv:1706.04465.
- 32. Nonjabulo, P.D.; Ngidi Ollengo, M.A.; Nyamori, V.O. Effect of doping temperatures and nitrogen precursors on the physicochemical, optical, and electrical conductivity properties of nitrogen-doped reduced graphene oxide. *Materials* **2019**, *12*, 3376.
- 33. Cançado, L.G.; Jorio, A.; Ferreira, E.M.; Stavale, F.; Achete, C.A.; Capaz, R.B.; Moutinho, M.V.O.; Lombardo, A.; Kulmala, T.S.; Ferrari, A.C. Quantifying defects in graphene via Raman spectroscopy at different excitation energies. *Nano Lett.* **2011**, *11*, 3190–3196. [CrossRef] [PubMed]
- 34. Wu, J.B.; Lin, M.L.; Cong, X.; Liu, H.N.; Tan, P.H. Raman spectroscopy of graphene-based materials and its applications in related devices. *Chem. Soc. Rev.* 2018, 47, 1822–1873. [CrossRef] [PubMed]
- 35. Das, A.; Pisana, S.; Piscanec, S.; Chakraborty, B.; Saha, S.K.; Waghmare, U.V.; Yiang, R.; Krishnamurhthy, H.R.; Keim, A.K.; Ferrari, A.C.; et al. Electrochemically top gated graphene: Monitoring dopants by Raman scattering. *arXiv* 2007, arXiv:0709.1174. [CrossRef]
- Casiraghi, C. Doping dependence of the Raman peaks intensity of graphene close to the Dirac point. Phys. Rev. B 2009, 80, 233407.
 [CrossRef]
- 37. Caridad, J.M.; Rossella, F.; Bellani, V.; Maicas, M.; Patrini, M.; Díez, E. Effects of particle contamination and substrate interaction on the Raman response of unintentionally doped graphene. *J. Appl. Phys.* **2010**, *108*, 84321. [CrossRef]
- 38. Boas, C.R.S.V.; Focassio, B.; Marinho, E.; Larrude, D.G.; Salvadori, M.C.; Leão, C.R.; Dos Santos, D.J. Characterization of nitrogen doped graphene bilayers synthesized by fast, low temperature microwave plasma-enhanced chemical vapour deposition. *Sci. Rep.* **2019**, *9*, 13715. [CrossRef]
- 39. Zhang, C.; Dabbs, D.M.; Liu, L.M.; Aksay, I.A.; Car, R.; Selloni, A. Combined effects of functional groups, lattice defects, and edges in the infrared spectra of graphene oxide. *J. Phys. Chem. C* **2015**, *119*, 18167–18176. [CrossRef]
- 40. Kakaei, K.; Esrafili, M.D.; Ehsani, A. Graphene Surfaces: Particles and Catalysts; Academic Press: Cambridge, MA, USA, 2018.
- 41. Milev, A.; Wilson, M.; Kannangara, G.K.; Tran, N. X-ray diffraction line profile analysis of nanocrystalline graphite. *Mater. Chem. Phys.* **2008**, *111*, 346–350. [CrossRef]
- Low, I.M.; Albetran, H.M.; Degiorgio, M. Structural characterization of commercial graphite and graphene materials. J. Nanotechnol. Nanomater. 2020, 1, 23–30.